

Topological Exciton Bands in Moiré Heterojunctions

Fengcheng Wu,^{1,2} Timothy Lovorn,¹ and A. H. MacDonald¹

¹*Department of Physics, University of Texas at Austin, Austin, TX 78712, USA*

²*Materials Science Division, Argonne National Laboratory, Argonne, IL 60439, USA*

(Dated: March 21, 2017)

Moiré patterns are common in van der Waals heterostructures and can be used to apply periodic potentials to elementary excitations. We show that the optical absorption spectrum of transition metal dichalcogenide bilayers is profoundly altered by long period moiré patterns that introduce twist-angle dependent satellite excitonic peaks. Topological exciton bands with non-zero Chern numbers that support chiral excitonic edge states can be engineered by combining three ingredients: i) the valley Berry phase induced by electron-hole exchange interactions, ii) the moiré potential, and iii) the valley Zeeman field.

Stacking two-dimensional (2D) materials into van der Waals heterostructures opens up new strategies for materials property engineering. One increasingly important example is the possibility of using the relative orientation (twist) angle between two 2D crystals to tune electronic properties. For small twist angles and lattice-constant mismatches, heterostructures exhibit long period moiré patterns that can yield dramatic changes. Moiré pattern formed in graphene-based heterostructures has been extensively studied, and many interesting phenomena have been observed, for example gap opening at graphene's Dirac point [1, 2], generation of secondary Dirac points[3, 4] and Hofstadter-butterfly spectra in a strong magnetic field[1, 5, 6].

In this Letter, we study the influence of moiré patterns on collective excitations, focusing on the important case of excitons in the transition metal dichalcogenide (TMD) 2D semiconductors [7, 8] like MoS₂ and WS₂. Exciton features dominate the optical response of these materials because electron-hole pairs are strongly bound by the Coulomb interaction [9–12]. An exciton inherits a pseudospin-1/2 valley degree of freedom from its constituent electron and hole, and the exciton valley pseudospin can be optically addressed [13–16], providing access to the valley Hall effect [17] and the valley selective optical Stark effect [18, 19].

As in the case of graphene/hexagonal-boron-nitride and graphene/graphene bilayers, a moiré pattern can be established in TMD bilayers by using two different materials with a small lattice mismatch, by applying a small twist, or by combining both effects. TMD heterostructures have been realized [20–22] experimentally and can host interesting effects, for example the observation of valley polarized interlayer excitons with long lifetimes [23], the theoretical prediction of multiple degenerate interlayer excitons [24], and the possibility of achieving spatially indirect exciton condensation [25, 26]. Our focus here is instead on the *intralayer* excitons that are more strongly coupled to light. As we explain below, the moiré pattern produces a periodic potential, mixing momentum states separated by moiré reciprocal lattice

vectors and producing satellite optical absorption peaks that are revealing. The exciton energy-momentum dispersion can be measured by tracking the dependence of satellite peak energies on twist angle.

The valley pseudospin of an exciton is intrinsically coupled to its center-of-mass motion by the electron-hole exchange interaction[27–30]. This effective spin-orbit coupling endows the exciton with a 2π momentum-space Berry phase[31]. We show that topological exciton bands characterized by quantized Chern numbers can be achieved by exploiting this momentum-space Berry phase combined with a periodic potential due to the moiré pattern and time-reversal symmetry breaking by a Zeeman field. All three ingredients are readily available in TMD bilayers. The bulk topological bands lead to chiral edge states, which can support unidirectional transport of excitons optically generated on the edge. Our study therefore suggests a practical new route to engineer topological collective excitations which are now actively sought[32–37] in several different contexts.

Exciton Potential Energy— For definiteness we consider the common chalcogen TMD bilayer MoX₂/WX₂ with a small twist angle θ and an in-plane displacement \mathbf{d} . TMDs with a common chalcogen (X) atom have small lattice mismatches ($\sim 0.1\%$), which we neglect to simplify calculations. Because of the van der Waals heterojunction character and relative band offsets, both conduction and valence bands of MoX₂ and WX₂ are weakly coupled across the heterojunction. The heterojunctions have two distinct stacking orders AA and AB, which are illustrated in Figs. 1(a) and 1(d). Both configurations have been experimentally realized [23, 38].

We start by analyzing the bilayer electronic structure at zero twist angle. Fully-relativistic density-functional-theory *ab initio* calculation is performed for crystalline MoS₂/WS₂ ($\theta = 0^\circ$) as a function of relative displacement \mathbf{d} . We used the local density approximation with optimized norm-conserving pseudopotentials [39, 40] as implemented in Quantum Espresso [41], and determined the orbital character of electronic bands using Wannier90 [42]. More details of the calculation are presented in the

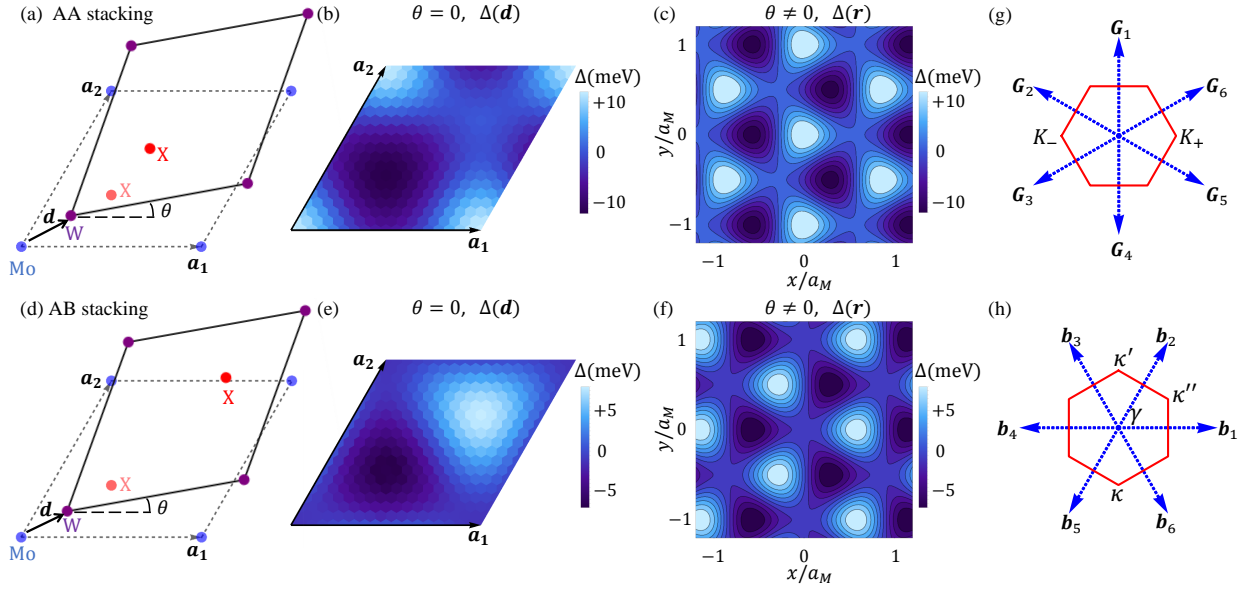


FIG. 1. (color online). (a) Illustration of AA stacking with a small twist angle θ and an in-plane displacement \mathbf{d} . (b) Variation of MoS₂ band gap as a function of \mathbf{d} in AA stacked MoS₂/WS₂ bilayer with zero twist angle. (c) Variation of MoS₂ band gap as a function of position in AB stacked twisted MoS₂/WS₂. (d)-(f) Corresponding plots for AB stacking. (g) First-shell reciprocal lattice vectors \mathbf{G}_j of a monolayer TMD triangular lattice and the corresponding Brillouin zone (red hexagon). (h) Moiré reciprocal lattice vectors and corresponding Brillouin zone

Supplemental Material [43]. Our primary interest here is intra-layer physics. Figs. 1(b) and 1(e) illustrate the \mathbf{d} dependence of the energy gap at the K_{\pm} points between states concentrated in the MoS₂ layer. The variation of the gap is a periodic function of \mathbf{d} with the 2D lattice periodicity, and is adequately approximated by the lowest harmonic expansion:

$$\Delta(\mathbf{d}) \equiv E_g(\mathbf{d}) - \langle E_g \rangle \approx \sum_{j=1}^6 V_j \exp(i\mathbf{G}_j \cdot \mathbf{d}), \quad (1)$$

where E_g is the intralayer band gap of MoS₂, $\langle E_g \rangle$ is its average over \mathbf{d} , and \mathbf{G}_j is a one of the first-shell reciprocal lattice vectors illustrated in Fig. 1(g). Three-fold rotational symmetry of the lattice leads to the constraint:

$$V_1 = V_3 = V_5, V_2 = V_4 = V_6. \quad (2)$$

Because Δ is real, we also have that $V_1 = V_4^*$. It follows that all six V_j are fixed by $V_1 = V \exp(i\psi)$. For MoS₂ on WS₂ we find that $(V, \psi) = (2.3\text{meV}, 30.8^\circ)$ for AA stacking and $(1.4\text{meV}, 98.6^\circ)$ for AB stacking. Because the band offset between the two layers can be modified by external electric fields, we expect that the values of these parameters can be tuned using gate voltages.

Rotation by angle θ transforms lattice vector \mathbf{L} to $\mathbf{L}' = \mathcal{R}(\theta)\mathbf{L}$, where $\mathcal{R}(\theta)$ is the rotation matrix. For small twist angles, the relative displacement[44] between two layers near position \mathbf{L}' is therefore,

$$\mathbf{d}(\mathbf{L}') = \hat{T}\mathbf{L}' = \hat{T}(\mathbf{L}' - \mathbf{L}) \approx \hat{T}(\theta\hat{z} \times \mathbf{L}'), \quad (3)$$

where the operator \hat{T} reduces a vector to the Wigner-Seitz cell of the triangular lattice labeled by \mathbf{L} . In the limit of small θ , the displacement varies smoothly with position. Because the size of an exciton in TMDs ($\sim 1\text{nm}$) is larger than the lattice constant scale, validating a $k \cdot p$ description, but much smaller than moiré periods, the influence of the displacement on exciton energy is local [45, 46]. We find that the variation in the band gap dominates over that of the binding energy[43]. For simplicity, we assume that the variation of exciton energy will follow that of local band gap:

$$\begin{aligned} \Delta(\mathbf{r}) &\approx \Delta(\mathbf{d}(\mathbf{r})) \approx \sum_{j=1}^6 V_j \exp(i\mathbf{G}_j \cdot \mathbf{d}(\mathbf{r})) \\ &\approx \sum_{j=1}^6 V_j \exp(i\mathbf{G}_j \cdot (\theta\hat{z} \times \mathbf{r})) = \sum_{j=1}^6 V_j \exp(i\mathbf{b}_j \cdot \mathbf{r}). \end{aligned} \quad (4)$$

Here $\Delta(\mathbf{r})$ acts as an exciton potential energy, and $\mathbf{b}_j = \theta\mathbf{G}_j \times \hat{z}$ defines the reciprocal lattice vectors of the moiré pattern. The band gap varies periodically in space due to the moiré pattern, as illustrated in Figs. 1(c) and 1(f). The moiré periodicity a_M is controlled by the twist angle: $a_M \approx a_0/\theta$, where a_0 is the lattice constant of a monolayer TMD.

Optical response.— We study the A exciton, the lowest-energy bright exciton, in monolayer MoS₂. Its low-energy

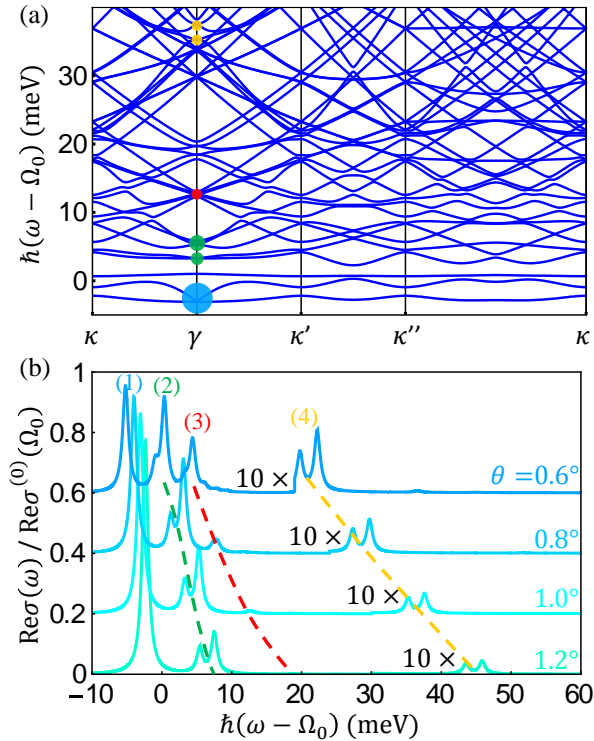


FIG. 2. (color online). (a) Exciton moiré bands along paths connecting high symmetry points in the MBZ. The twist angle θ used for this calculation is 1° . The sizes of the dots at the γ point correspond to the weight of state $|K_{\pm}^{(0)}\rangle$. The color of the dots encodes the main character of the states, with blue, red, green and yellow corresponding to character (1), (2), (3) and (4). See text. (b) Optical conductivity at several twist angles θ . Curves for different θ are shifted vertically for clarity and the dashed curves track the peak evolution. The two mini-peaks in (4) are amplified ten times. The broadening factor η is taken to be 0.5meV . The exciton potential parameters of AA stacked MoS_2/WS_2 were used in these calculations.

effective Hamiltonian [27–30] is:

$$H_0 = (\hbar\Omega_0 + \frac{\hbar^2\mathbf{Q}^2}{2M})\tau_0 + J|\mathbf{Q}|\tau_0 + J|\mathbf{Q}|\left[\cos(2\phi_{\mathbf{Q}})\tau_x + \sin(2\phi_{\mathbf{Q}})\tau_y\right], \quad (5)$$

where \mathbf{Q} is exciton momentum, $\hbar\Omega_0$ is its $\mathbf{Q} = 0$ energy, $\hbar^2\mathbf{Q}^2/(2M)$ is its center-of-mass kinetic energy, and τ_0 and $\tau_{x,y}$ are respectively identity matrix and Pauli matrices in valley space. In Eq. (5), $\phi_{\mathbf{Q}}$ is the orientation angle of the 2D vector \mathbf{Q} , $J|\mathbf{Q}|\tau_0$ accounts for intravalley electron-hole exchange interactions, and the $\tau_{x,y}$ terms account for their intervalley counterparts[47]. It follows that the A exciton has two energy modes,

$$E_{\pm}(\mathbf{Q}) = \hbar\Omega_0 + \frac{\hbar^2\mathbf{Q}^2}{2M} + J|\mathbf{Q}| \pm J|\mathbf{Q}|. \quad (6)$$

Note that E_+ has linear dispersion at small $|\mathbf{Q}|$, while the lower mode E_- is quadratic. From the *ab initio*

GW Bethe-Salpeter calculation of Ref. [48] we obtain $M = 1.3m_0$ and $J = 0.4\text{eV} \cdot \text{\AA}$, where m_0 is the free electron mass. Since the gap variation is guaranteed by time reversal symmetry to be identical for K_+ and K_- valleys, the exciton effective Hamiltonian of twisted bilayers is $H = H_0 + \Delta(\mathbf{r})\tau_0$.

We numerically diagonalize the Hamiltonian matrix using a plane-wave expansion; exciton momentum reduced to the moiré Brillouin zone (MBZ) is a good quantum number. Fig. 2(a) illustrates the MoS_2 A exciton moiré bands for a 1° twist relative to WS_2 . Smaller twist angles imply smaller MBZ dimensions and more moiré bands in a given energy window. For twist angles $\theta > 0.5^\circ$, the wavelength (640nm) of light that excites A excitons greatly exceeds the moiré periodicity ($< 36\text{nm}$). It follows that only excitons close to the MBZ center γ are optically active. The real part of the optical conductivity can be expressed as follows,

$$\begin{aligned} \text{Re}\sigma(\omega) &= \frac{1}{\omega\mathcal{A}} \sum_n |\langle\chi_n|j_x|G\rangle|^2 \Gamma_1(\omega - \omega_n) \\ &\approx \frac{|\langle K_+^{(0)}|j_x|G\rangle|^2}{\omega\mathcal{A}} \sum_n \left| \sum_{\alpha=\pm} \langle\chi_n|K_{\alpha}^{(0)}\rangle \right|^2 \Gamma_1(\omega - \omega_n) \quad (7) \\ &\approx \frac{1}{2} \text{Re}\sigma^{(0)}(\Omega_0) \sum_n \left| \sum_{\alpha=\pm} \langle\chi_n|K_{\alpha}^{(0)}\rangle \right|^2 \Gamma_2(\omega - \omega_n), \end{aligned}$$

where \mathcal{A} is the system area, $\Gamma_m(\omega - \omega_n) = \eta^m / [\hbar^2(\omega - \omega_n)^2 + \eta^2]$ and η is a broadening parameter. In Eq. (7) j_x is the current operator, $|G\rangle$ is the neutral semiconductor ground state, $|\chi_n\rangle$ and $\hbar\omega_n$ are the eigenstates and eigenvalues of the exciton moiré Hamiltonian at the γ point, $|K_{\alpha}^{(0)}\rangle$ is the valley K_{α} exciton eigenstate at zero twist angle, and $\text{Re}\sigma^{(0)}(\Omega_0)$ is the A exciton optical conductivity peak also at zero twist angle. The assumption underlying Eq. (7) is that only the $|K_{\pm}^{(0)}\rangle$ component in $|\chi_n\rangle$ contributes to the optical response. The final form for $\sigma(\omega)$ emphasizes that the exciton moiré potential has the effect of redistributing the A -exciton peak over a series of closely spaced sub-peaks.

Theoretical optical conductivities for a series of twist angles are illustrated in Fig. 2(b). Peaks labelled (1-4) (see caption) correspond respectively to bare excitons at zero momentum, E_- excitons at momentum \mathbf{b}_i , E_- excitons at momentum $\sqrt{3}\mathbf{b}_i \times \hat{z}$, and E_+ excitons at momentum \mathbf{b}_i . Without the moiré pattern there would only be one peak centered around frequency Ω_0 ; umklapp scattering off the moiré potentials unveils the formerly dark finite-momentum excitonic states. Both (2) and (4) give rise to two mini-peaks with a small energy splitting. As the twist angle decreases, $|\mathbf{b}_i|$ is reduced and the satellite peaks shift to lower energy and become stronger; for $\theta \sim 0.6^\circ$ satellite peaks (2) and (3) have strength that is comparable to that of peak (1). Although peak (4) is weak, it decays more slowly compared to peak (3) when θ increases. The energy difference between peak (2) and

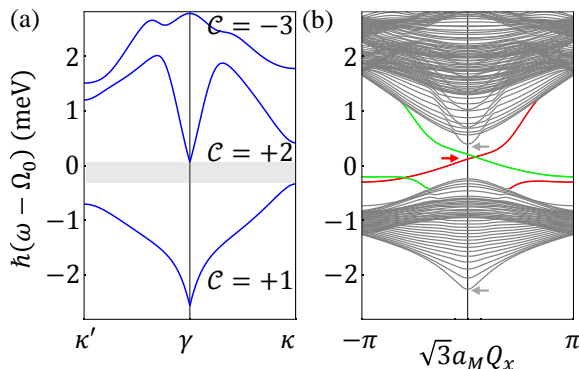


FIG. 3. (color online). (a) Topological exciton bands with quantized Chern numbers \mathcal{C} for twist angle $\theta = 1^\circ$. The gray bar identifies the gap between the first and second exciton moiré bands. (b) Stripe geometry quasi-1D bands for the same twist angle, an extended edge along the x direction, and finite width in the y direction. The red and green lines show the dispersions of chiral exciton states that are localized on opposite edges of the stripe. In (a) and (b), h_z is 1.5meV, and (V, ψ) take the parameter values of AB stacked MoS₂/WS₂.

(4) provides a direct measurement of the electron-hole exchange interaction strength.

Topological excitons.—The intervalley exchange interaction acts as an in-plane valley-space pseudo-magnetic field which rotates by 4π when the momentum encloses its origin once. This non-trivial winding number can be used to engineer topological exciton bands when combined with the moiré superlattice potential, which provides a finite Brillouin zone and an energy gap above the lowest exciton band at every \mathbf{Q} point in the MBZ except the γ point. An external Zeeman term $h_z\tau_z$ can split the degeneracy at γ . A Zeeman term of this form has been experimentally realized in monolayer TMDs by applying a magnetic field [49–51] and by using a valley selective optical Stark effect [18, 19]. The topology of the exciton bands is characterized by Berry curvature \mathcal{F} and Chern number \mathcal{C} , just as in the electronic case:

$$\begin{aligned} \mathcal{F}_n(\mathbf{Q}) &= \hat{z} \cdot \nabla_{\mathbf{Q}} \times [i\langle \chi_n(\mathbf{Q}) | \nabla_{\mathbf{Q}} | \chi_n(\mathbf{Q}) \rangle], \\ \mathcal{C}_n &= \int_{\text{MBZ}} \frac{d^2\mathbf{Q}}{2\pi} \mathcal{F}_n(\mathbf{Q}), \end{aligned} \quad (8)$$

where $|\chi_n(\mathbf{Q})\rangle$ represents the n th eigenstate of Hamiltonian H at momentum \mathbf{Q} . Fig. 3(a) presents our results for the topological properties of moiré exciton bands in AB stacked MoS₂/WS₂. We find that the first exciton band can possess a non-zero Chern number, and that it is isolated from other bands by a global energy gap. The corresponding Berry curvature \mathcal{F} has hot spots around γ , κ , and κ' points in the MBZ. \mathcal{F} around γ is simply understood in terms of the valley Berry phase induced by the exchange interaction, and its sign is determined by that of h_z . The peak in \mathcal{F} around the κ and κ' point is related to gap opening due to moiré pattern, and can

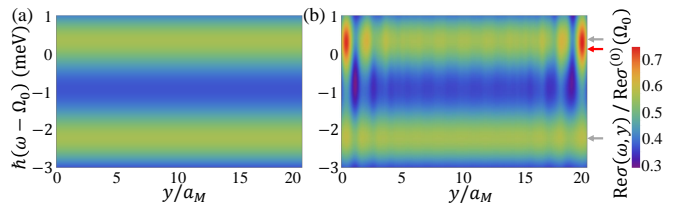


FIG. 4. (color online). Spatially resolved optical conductivity on the same stripe geometry as studied in Fig. 3(b). The optical conductivity is averaged over x . (a) Response from bulk states. The energy splitting between the two peaks is due to the Zeeman energy. An energy broadening factor of 1meV is used. (b) Response from both bulk and edge states. There is an enhancement of the optical response around the edge due to edge states. The arrows indicate the energy level of bulk states (gray arrow) and edge state (red arrow) in the absence of energy broadening, and correspond to the three arrows shown in Fig. 3(b).

vary as a function of ψ , the phase of V_1 . We find that the Chern number is finite in a large parameter space of (ψ, θ) [43]. Therefore we expect that topological exciton bands appear routinely in TMD bilayers.

Chiral excitonic edge states expected for topological bands are confirmed by studying the energy spectrum of a finite-width stripe [43], as illustrated in Fig. 3(b). These states can support unidirectional excitonic transport channels. We have computed optical response of the edge states[43]. The spatially resolved optical conductivity is shown in Fig. 4. Based on numerical results, we find that the *maximum* local optical conductivity due to one edge state is about $0.19\text{Re}\sigma^{(0)}(\Omega_0)$, which is comparable in magnitude to that of the bulk states. As illustrated in Fig. 4(b), edge states give rise to enhanced response around the edge, and therefore can be detected by spatially resolved absorption spectroscopy.

In summary, intralayer excitons in a twisted TMD bilayer exhibit rich phenomena enabled by the moiré pattern, including satellite excitonic peaks in optical absorption peaks that are tunable by varying twist angle. The moiré superlattice potential, the exciton Zeeman field, and the electron-hole exchange induced valley Berry phase can in combination give rise to topological exciton bands. Our analysis points to a practical strategy to realize topological excitons.

We would like to thank Feng Wang and Ivar Martin for useful discussions. Work at Austin was supported by the Department of Energy, Office of Basic Energy Sciences under contract DE-FG02-ER45118 and award # DE-SC0012670, and by the Welch foundation under grant TBF1473. Work of FW at Argonne was supported by the Department of Energy, Office of Science, Materials Sciences and Engineering Division. We acknowledge computer time allocations from Texas Advanced Computing Center.

-
- [1] B. Hunt *et al.*, *Science* **340**, 1427 (2013).
- [2] E. Wang *et al.*, *Nat. Phys.* **12**, 1111 (2016).
- [3] M. Yankowitz, J. Xue, D. Cormode, J. D. Sanchez-Yamagishi, K. Watanabe, T. Taniguchi, P. Jarillo-Herrero, P. Jacquod, and B. J. LeRoy, *Nat. Phys.* **8**, 382 (2012).
- [4] L. Ponomarenko *et al.*, *Nature* **497**, 594 (2013).
- [5] C. Dean *et al.*, *Nature* **497**, 598 (2013).
- [6] K. Kim, A. DaSilva, S. Huang, B. Fallahazad, S. Larentis, T. Taniguchi, K. Watanabe, B. J. LeRoy, A. H. MacDonald, and E. Tutuc, *PNAS*, in press(2017) .
- [7] A. Splendiani, L. Sun, Y. Zhang, T. Li, J. Kim, C.-Y. Chim, G. Galli, and F. Wang, *Nano Lett.* **10**, 1271 (2010).
- [8] K. F. Mak, C. Lee, J. Hone, J. Shan, and T. F. Heinz, *Phys. Rev. Lett.* **105**, 136805 (2010).
- [9] Z. Ye, T. Cao, K. O'Brien, H. Zhu, X. Yin, Y. Wang, S. G. Louie, and X. Zhang, *Nature* **513**, 214 (2014).
- [10] K. He, N. Kumar, L. Zhao, Z. Wang, K. F. Mak, H. Zhao, and J. Shan, *Phys. Rev. Lett.* **113**, 026803 (2014).
- [11] A. Chernikov, T. C. Berkelbach, H. M. Hill, A. Rigosi, Y. Li, O. B. Aslan, D. R. Reichman, M. S. Hybertsen, and T. F. Heinz, *Phys. Rev. Lett.* **113**, 076802 (2014).
- [12] D. Y. Qiu, F. H. da Jornada, and S. G. Louie, *Phys. Rev. Lett.* **111**, 216805 (2013).
- [13] T. Cao, G. Wang, W. Han, H. Ye, C. Zhu, J. Shi, Q. Niu, P. Tan, E. Wang, B. Liu, *et al.*, *Nat. Commun.* **3**, 887 (2012).
- [14] H. Zeng, J. Dai, W. Yao, D. Xiao, and X. Cui, *Nat. Nanotechnol.* **7**, 490 (2012).
- [15] K. F. Mak, K. He, J. Shan, and T. F. Heinz, *Nat. Nanotechnol.* **7**, 494 (2012).
- [16] D. Xiao, G.-B. Liu, W. Feng, X. Xu, and W. Yao, *Phys. Rev. Lett.* **108**, 196802 (2012).
- [17] K. F. Mak, K. L. McGill, J. Park, and P. L. McEuen, *Science* **344**, 1489 (2014).
- [18] J. Kim, X. Hong, C. Jin, S.-F. Shi, C.-Y. S. Chang, M.-H. Chiu, L.-J. Li, and F. Wang, *Science* **346**, 1205 (2014).
- [19] E. J. Sie, J. W. McIver, Y.-H. Lee, L. Fu, J. Kong, and N. Gedik, *Nat. Mat.* **14**, 290 (2015).
- [20] H. Fang *et al.*, *PNAS* **111**, 6198 (2014).
- [21] Y. Gong *et al.*, *Nat. Mat.* **13**, 1135 (2014).
- [22] K. Liu, L. Zhang, T. Cao, C. Jin, D. Qiu, Q. Zhou, A. Zettl, P. Yang, S. G. Louie, and F. Wang, *Nat. Commun.* **5**, 4966 (2014).
- [23] P. Rivera, K. L. Seyler, H. Yu, J. R. Schaibley, J. Yan, D. G. Mandrus, W. Yao, and X. Xu, *Science* **351**, 688 (2016).
- [24] H. Yu, Y. Wang, Q. Tong, X. Xu, and W. Yao, *Phys. Rev. Lett.* **115**, 187002 (2015).
- [25] M. Fogler, L. Butov, and K. Novoselov, *Nat. Commun.* **5** (2014).
- [26] F.-C. Wu, F. Xue, and A. H. MacDonald, *Phys. Rev. B* **92**, 165121 (2015).
- [27] H. Yu, G.-B. Liu, P. Gong, X. Xu, and W. Yao, *Nat. Commun.* **5** (2014).
- [28] M. M. Glazov, T. Amand, X. Marie, D. Lagarde, L. Bouet, and B. Urbaszek, *Phys. Rev. B* **89**, 201302 (2014).
- [29] T. Yu and M. W. Wu, *Phys. Rev. B* **89**, 205303 (2014).
- [30] F. Wu, F. Qu, and A. H. MacDonald, *Phys. Rev. B* **91**, 075310 (2015).
- [31] The effect of the exchange interaction on spatially indirect excitons has been discussed, for example, in Ref. [52].
- [32] J. Yuen-Zhou, S. K. Saikin, N. Y. Yao, and A. Aspuru-Guzik, *Nat. Mat.* **13**, 1026 (2014).
- [33] T. Karzig, C.-E. Bardyn, N. H. Lindner, and G. Refael, *Phys. Rev. X* **5**, 031001 (2015).
- [34] C.-E. Bardyn, T. Karzig, G. Refael, and T. C. H. Liew, *Phys. Rev. B* **91**, 161413 (2015).
- [35] A. V. Nalitov, D. D. Solnyshkov, and G. Malpuech, *Phys. Rev. Lett.* **114**, 116401 (2015).
- [36] J. C. W. Song and M. S. Rudner, *PNAS* **113**, 4658 (2016).
- [37] D. Jin, L. Lu, Z. Wang, C. Fang, J. D. Joannopoulos, M. Soljačić, L. Fu, and N. X. Fang, *Nat. Commun.* **7**, 13486 (2016).
- [38] N. R. Wilson *et al.*, *Sci. Adv.* **3**, e1601832 (2017).
- [39] D. R. Hamann, *Phys. Rev. B* **88**, 085117 (2013).
- [40] M. Schlipf and F. Gygi, *Comput. Phys. Commun.* **196**, 36 (2015).
- [41] P. Giannozzi *et al.*, *J. Phys.: Condens. Matter* **21**, 395502 (2009).
- [42] A. A. Mostofi, J. R. Yates, G. Pizzi, Y.-S. Lee, I. Souza, D. Vanderbilt, and N. Marzari, *Comput. Phys. Commun.* **185**, 2309 (2014).
- [43] See Supplemental Material for details of *ab initio* calculations, discussion on local approximation, topological phase diagram and edge state analysis. It includes Refs. [53–56].
- [44] Bulk properties of moiré systems with finite twist angle are independent of the relative displacement prior to twist which we set to zero. See Ref. 57 for an explanation.
- [45] M. Wu, X. Qian, and J. Li, *Nano Lett.* **14**, 5350 (2014).
- [46] J. Jung, A. Raoux, Z. Qiao, and A. H. MacDonald, *Phys. Rev. B* **89**, 205414 (2014).
- [47] We used static approximation for the exchange interaction. Retardation effect results in intrinsic energy broadening of exciton states in the light cone. See Ref. [28].
- [48] D. Y. Qiu, T. Cao, and S. G. Louie, *Phys. Rev. Lett.* **115**, 176801 (2015).
- [49] D. MacNeill, C. Heikes, K. F. Mak, Z. Anderson, A. Kormányos, V. Zólyomi, J. Park, and D. C. Ralph, *Phys. Rev. Lett.* **114**, 037401 (2015).
- [50] A. Srivastava, M. Sidler, A. V. Allain, D. S. Lembke, A. Kis, and A. Imamoglu, *Nat. Phys.* **11**, 141 (2015).
- [51] G. Aivazian, Z. Gong, A. M. Jones, R.-L. Chu, J. Yan, D. G. Mandrus, C. Zhang, D. Cobden, W. Yao, and X. Xu, *Nat. Phys.* **11**, 148 (2015).
- [52] M. V. Durnev and M. M. Glazov, *Phys. Rev. B* **93**, 155409 (2016).
- [53] J. P. Perdew and A. Zunger, *Phys. Rev. B* **23**, 5048 (1981).
- [54] F. A. Rasmussen and K. S. Thygesen, *J. Phys. Chem. C* **119**, 13169 (2015).
- [55] W. S. Yun, S. W. Han, S. C. Hong, I. G. Kim, and J. D. Lee, *Phys. Rev. B* **85**, 033305 (2012).
- [56] A. D. Corso, *Computational Materials Science* **95**, 337 (2014).
- [57] R. Bistritzer and A. H. MacDonald, *PNAS* **108**, 12233 (2011).

Supplemental Material

DETAILS OF THE *AB INITIO* CALCULATION

We perform fully-relativistic density functional theory (DFT) calculations under the local-density approximation (LDA) [53] for the MoS₂/WS₂ bilayer system using the Quantum Espresso distribution [41]. We use norm-conserving pseudopotentials based on those provided by the SG15 pseudopotential library [40]; this library provides optimized inputs for the ONCVSP pseudopotential generation method [39]. We alter the pseudopotential generation inputs from the SG15 library to produce fully-relativistic, LDA pseudopotentials; the cutoff radius of the *W* *p* states is also reduced slightly to eliminate a ghost state which appears when converting the pseudopotential to fully-relativistic LDA.

Lattice structures for the MoS₂ and WS₂ layers are taken from Ref. [54]. We take the interlayer distance to be that of bulk MoS₂ as given by Ref. [55] and choose a 20Å vacuum distance for the slab model. We choose a plane-wave cutoff energy of 60 Ry and corresponding charge density cutoff energy of 240 Ry, and we sample the Brillouin zone with a 9×9×1 grid of *k* points. The gap values obtained using this cutoff energy and *k*-space grid are found to be well-converged relative to calculations at twice the cutoff energy and at twice the number of *k* points in each direction. The variation of the overall band gap with *d* is also found to be consistent with a calculation in which we replaced the norm-conserving pseudopotentials with projector augmented wave (PAW) data sets from PSLibrary 1.0.0 [56].

To determine the orbital character of electronic bands, we obtain a tight-binding Hamiltonian in a basis of Wannier functions using Wannier90 [42]. We project onto *p* orbitals for S and *d* orbitals for Mo and W, and reproduce the DFT band structure with high accuracy. Disentanglement is necessary due to a small overlap in energy between the group of conduction bands and higher states; we do not perform maximal localization. The gap between valence and conduction bands for MoS₂ states at the *K* point (shown in Fig. 1(b,e) of the main text) is calculated by considering states with total weight greater than a threshold value of 0.7 on the MoS₂ layer. We find that the states nearest the Fermi energy at the *K* point are strongly layer-selective, with the gap value obtained by this procedure being independent of this threshold in the range 0.05 to 0.85 for both AA and AB stacking.

The software used to generate inputs for Quantum Espresso and Wannier90 and to calculate gaps in MoS₂-dominated states from the *ab initio* result is available at <https://github.com/tflovrn/tmd>.

It is known that LDA underestimates the band gap for semiconductors like MoS₂. We view our work as a qualitative instead of quantitative study, and expect that the

effects discussed in the main text are generic. Moreover our strategy for estimating the exciton moiré potential strength can accommodate more accurate approaches, like GW calculation and GW Bethe-Salpeter calculation.

LOCAL APPROXIMATION FOR EXCITON MOIRÉ POTENTIAL

In this section we discuss the local approximation we use for the influence of substrate registration on the exciton Hamiltonian. There are three length scales in the problem: the lattice constant a_0 , the exciton size a_X and the moiré periodicity a_M . For MoS₂, a_0 is about 3.19Å. The moiré length $a_M = a_0/\theta$ is about 20nm for a typical twist angle θ around 1°. We can approximate a_X by the root of mean square of the electron-hole separation in the *A* exciton state of MoS₂. The exciton wave function is obtained by solving the Bethe-Salpeter equation based on massive Dirac model. The details of this microscopic model can be found in Appendix B of Ref.[30]. a_X depends on dielectric constant ϵ . From that calculation, we find that a_X is 1.05nm, 1.15nm and 1.3nm respectively for $\epsilon = 1, 2.5$ and 4. Note that monolayer MoS₂ is two dimensional, and its dielectric constant is mainly determined by its environment. For example ϵ is about 4 when the twisted bilayer is encapsulated by hexagonal boron nitride. As ϵ increases, the Coulomb interaction becomes weaker and meantime the local screening effect from the 2D material itself also becomes weaker[30]. This is the reason why a_X does not scale linearly with ϵ .

Because $a_X > a_0$, a $k \cdot p$ description of exciton is justified. As a_M is much larger than a_X and the band gap varies smoothly on the scale of a_M , it is a good approximation to assume that the variation of exciton energy is determined by the local band gap and band edge mass parameters.

The exciton energy is $E_g - E_b$, where E_g and E_b are respectively band gap and exciton binding energy. We have obtained the variation in E_g from *ab initio* calculation as reported in the main text. We now provide an estimate of the spatial variation of E_b . In $k \cdot p$ theory E_b scales linearly with the reduced mass $\mu = m_c m_v / (m_c + m_v)$, where m_c and m_v are respectively the conduction and valence band effective mass. μ has been calculated as a function of the relative displacement *d* based on DFT band structure. The numerical results show that μ has a variation about $\pm 0.5\%$, which leads to a similar relative variation in E_b . It is known that E_b in monolayer TMDs is relatively large and on the order of few hundred meV[9–12, 30]. The exact value of E_b depends on the dielectric constant ϵ . If we estimate E_b as 400meV, then the variation of E_b due to moiré pattern is about ± 2 meV. Note that the variation of E_g is about ± 10 meV, as shown in Fig. 1(b) and (e) in the main text. From this estimation, we argue that the variation of E_g dominates

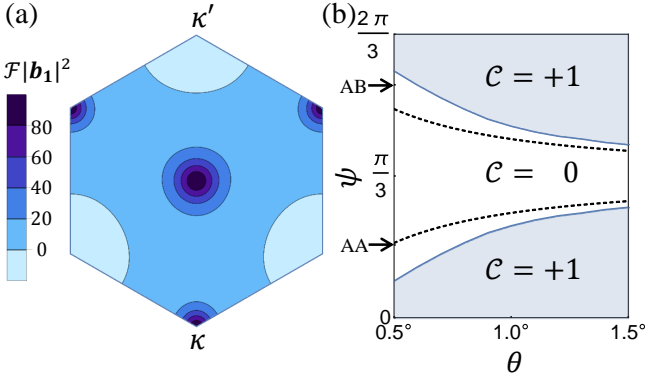


FIG. 5. (color online). (a) Berry curvature \mathcal{F} of the first band in Fig. 3(a) of the main text. \mathcal{F} is calculated using the Kubo formula expression. (b) Chern number \mathcal{C} of the first exciton moiré band as a function of θ and ψ with (V, h_z) fixed at $(1.4\text{meV}, 1.5\text{meV})$. The arrows indicate the value of ψ in AA and AB stacked MoS₂/WS₂. Adding $2\pi/3$ to ψ leads to a spatial translation of the moiré pattern. It follows that \mathcal{C} is a periodic function of ψ with periodicity $2\pi/3$. Dashed lines mark analytic but approximate phase boundaries determined by (16) and (17).

over that of E_b . With this justification we neglect the variation in E_b .

We emphasize that the parametrization of $\Delta(\mathbf{r})$, i.e. the exciton energy variation in moiré pattern, in Eq.(4) of the main text results from the three-fold rotational symmetry of the lattice structure and the smoothness of moiré potential. The parametrization of $\Delta(\mathbf{r})$ in terms of two parameters (V, ψ) is valid independent of the microscopic origin of the exciton energy variation.

TOPOLOGICAL PHASE DIAGRAM

The Berry curvature \mathcal{F} of the first exciton band in Fig. 3(b) of the main text is shown in Fig. 5(a), which displays hot spots around γ , κ , and κ' points in the MBZ. \mathcal{F} around γ is simply understood in terms of the valley Berry phase induced by the exchange interaction, and its sign is determined by that of h_z . The peak in \mathcal{F} around the κ and κ' point is related to gap opening in moiré pattern, and can be sensitive to ψ , the phase of V_1 . To test how robust the topological exciton band is, we calculate the Chern number of the first band as a function of ψ and twist angle θ . The resulting topological phase diagram is shown in Fig. 5(b). Because the Chern number is finite in a large parameter space of (ψ, θ) , we expect that there is a good chance that topological exciton bands can be realized in TMD bilayers. Along the phase boundary lines at which the Chern number changes, the energy gaps at κ or κ' close. Below we show that the phase boundaries can be qualitatively captured by treating the moiré potential as a perturbation.

In the absence of the moiré pattern, there are two energy modes at each momentum. The wave function of the lower mode at momentum \mathbf{Q} can be expressed as a two-component spinor in the valley space:

$$|\mathbf{Q}\rangle = \begin{pmatrix} \sin(\frac{\alpha\mathbf{Q}}{2}) \\ -\cos(\frac{\alpha\mathbf{Q}}{2})e^{i2\phi\mathbf{Q}} \end{pmatrix}, \quad (9)$$

where $\alpha\mathbf{Q}$ is determined by the condition:

$$\cos(\alpha\mathbf{Q}) = \frac{h_z}{\sqrt{h_z^2 + (J|\mathbf{Q}|)^2}}. \quad (10)$$

The moiré potential couples states with momenta that differ by a moiré reciprocal lattice vector. At the κ point of the moiré Brillouine zone, the three lowest energy states mainly originate from $|\mathbf{q}_i\rangle$, the lower energy modes at momenta \mathbf{q}_i , which are illustrated in Fig. 6(a). The three lowest energy states at κ would be degenerate if the moiré potential vanishes. The potential lifts the degeneracy, and can be treated by degenerate state perturbation theory. The potential projected to $|\mathbf{q}_i\rangle$ has the matrix form:

$$\begin{aligned} \mathcal{V}_\kappa &= \begin{pmatrix} 0 & V_5\langle\mathbf{q}_1|\mathbf{q}_2\rangle & V_6\langle\mathbf{q}_1|\mathbf{q}_3\rangle \\ V_2\langle\mathbf{q}_2|\mathbf{q}_1\rangle & 0 & V_1\langle\mathbf{q}_2|\mathbf{q}_3\rangle \\ V_3\langle\mathbf{q}_3|\mathbf{q}_1\rangle & V_4\langle\mathbf{q}_3|\mathbf{q}_2\rangle & 0 \end{pmatrix} \\ &= \frac{V}{2} \begin{pmatrix} 0 & \lambda & \lambda^* \\ \lambda^* & 0 & \lambda \\ \lambda & \lambda^* & 0 \end{pmatrix}, \end{aligned} \quad (11)$$

where parameter λ is:

$$\lambda = e^{i\psi}[e^{-i\pi/3} - \beta e^{i\pi/6}], \quad \beta = \frac{\sqrt{3}h_z}{\sqrt{h_z^2 + (J|\mathbf{q}_1|)^2}}. \quad (12)$$

Note that ψ is the phase of V_1 , and $|\mathbf{q}_1| = 4\pi/(3a_M) = 4\theta\pi/(3a_0)$. Therefore $|\mathbf{q}_1|$ is controlled by the twist angle θ .

κ is a high symmetry point. In particular, it is invariant under a three-fold rotational symmetry. Due to this symmetry, \mathcal{V}_κ commutes with the following cyclic permutation matrix \hat{C}_3 :

$$\hat{C}_3 = \begin{pmatrix} 0 & 1 & 0 \\ 0 & 0 & 1 \\ 1 & 0 & 0 \end{pmatrix}. \quad (13)$$

Thus \mathcal{V}_κ and \hat{C}_3 can be diagonalized simultaneously:

$$\begin{aligned} \mathcal{V}_\kappa|n\rangle &= \epsilon_n|n\rangle, \\ \hat{C}_3|n\rangle &= e^{i2n\pi/3}|n\rangle, \end{aligned} \quad (14)$$

where n takes integer values -1, 0 and +1. The eigen states and energies are respectively:

$$\begin{aligned} |n\rangle &= \frac{1}{\sqrt{3}} \begin{pmatrix} e^{i2n\pi/3} \\ e^{-i2n\pi/3} \\ 1 \end{pmatrix}, \\ \epsilon_n/V &= -\sqrt{1 + \beta^2} \cos[\psi + (n+1)\frac{2\pi}{3} - \arctan\beta]. \end{aligned} \quad (15)$$

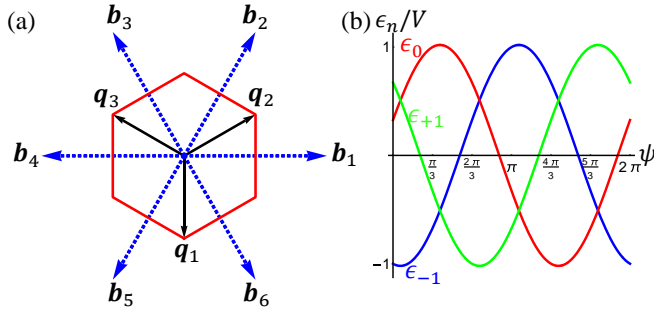


FIG. 6. (color online). (a) Due to the moiré potential, states at three different momenta \mathbf{q}_i are folded to the same point κ . (b) ϵ_n as a function ψ at $\beta = 0.2$.

Fig. 6(b) plots ϵ_n as a function of ψ for a non-zero β [defined in Eq. (12)]. Because of the symmetry \hat{C}_3 , there are level crossings (instead of avoided crossing) between different states. If we consider ψ in the range $(0, 2\pi/3)$ and assume h_z is small, the gap between the lowest energy state and higher energy states at κ closes when ϵ_{-1} equals ϵ_{+1} . This leads to the κ point gap closing condition:

$$\psi = \pi/3 + \arctan \beta. \quad (16)$$

In the same manner, we find the gap closing condition at κ' point is:

$$\psi = \pi/3 - \arctan \beta. \quad (17)$$

Note that when $h_z = 0$, β vanishes and the gap at κ and κ' close simultaneously, which is a result of time reversal symmetry. The analytic phase boundaries presented by Eqs. (16) and (17) correctly capture the trend of the numerical phase boundaries, as shown in Fig. 5(b).

ENERGY SPECTRUM OF A STRIPE

To study edge states, we consider a stripe with finite width L_y in y direction. We use a hard-wall boundary condition, which requires the wave function to vanish at the two edges, $y = 0$ and $y = L_y$. This boundary condition leads to the basis states:

$$|Q_x, n, \alpha\rangle = \sqrt{\frac{2}{\mathcal{A}}} \sin\left(\frac{n\pi}{L_y}y\right) \exp(iQ_x x) |\alpha\rangle, \quad (18)$$

where \mathcal{A} is the area of the stripe and n takes positive integer numbers. $|\alpha\rangle$ represents valley K_+ or K_- exciton.

We decompose the Hamiltonian into different terms:

$$\begin{aligned} H &= \hat{h}_0 + \hat{h}_x + \hat{h}_y + \hat{h}_z + \sum_{j=1}^6 \tilde{V}_j \exp(i\mathbf{b}_j \cdot \mathbf{r}) \tau_0, \\ \hat{h}_0 &= (\hbar\Omega_0 + \frac{\hbar^2 \mathbf{Q}^2}{2M} + J|\mathbf{Q}|) \tau_0, \\ \hat{h}_x &= J|\mathbf{Q}| \cos(2\phi_{\mathbf{Q}}) \tau_x, \quad \hat{h}_y = J|\mathbf{Q}| \sin(2\phi_{\mathbf{Q}}) \tau_y, \\ \hat{h}_z &= h_z \tau_z, \quad \tilde{V}_j = V_j \exp(-i\mathbf{b}_j \cdot \mathbf{l}), \end{aligned} \quad (19)$$

where \mathbf{Q} is understood to be an operator, and its eigenstates are plane waves. The vector \mathbf{l} describes the spatial translation of the moiré pattern, which is not important for the bulk energy spectrum. However, it determines where the edge at $y = 0$ is located in the moiré unit cell. \mathbf{l} can be varied to tune the energy dispersion of states localized on the $y = 0$ edge.

The Hamiltonian matrix element in the basis $|Q_x, n, \alpha\rangle$ is specified as follows:

$$\begin{aligned} \langle Q_x, n, \alpha | \hat{h}_0 + \hat{h}_z | Q'_x, n', \alpha' \rangle &= \delta_{Q_x Q'_x} \delta_{nn'} \delta_{\alpha\alpha'} [\hbar\Omega_0 + \frac{\hbar^2 \mathbf{Q}^2}{2M} + J|\mathbf{Q}| + h_z \tau_z^{(\alpha\alpha')}], \\ \langle Q_x, n, \alpha | \hat{h}_x | Q'_x, n', \alpha' \rangle &= \delta_{Q_x Q'_x} \delta_{nn'} J|\mathbf{Q}| \cos(2\phi_{\mathbf{Q}}) \tau_x^{(\alpha\alpha')}, \\ \langle Q_x, n, \alpha | \hat{h}_y | Q'_x, n', \alpha' \rangle &= \delta_{Q_x Q'_x} J \left(\frac{Q_x}{\sqrt{(L_y Q_x)^2 + (n\pi)^2}} + \frac{Q_x}{\sqrt{(L_y Q_x)^2 + (n'\pi)^2}} \right) f(n, n') \tau_y^{(\alpha\alpha')}, \\ \langle Q_x, n, \alpha | \exp(i\mathbf{b} \cdot \mathbf{r}) \tau_0 | Q'_x, n', \alpha' \rangle &= \delta_{Q_x - Q'_x, b_x} \delta_{\alpha\alpha'} \frac{1}{2} \left[F(b_y L_y / \pi + n - n') \right. \\ &\quad \left. - F(b_y L_y / \pi + n + n') - F(b_y L_y / \pi - n - n') \right], \end{aligned} \quad (20)$$

where \mathbf{Q} represents the vector $(Q_x, \frac{n\pi}{L_y})$, and the two

functions are:

$$\begin{aligned} f(n, n') &= -i\pi n' \frac{2}{L_y} \int_0^{L_y} \sin\left(\frac{n\pi}{L_y}y\right) \cos\left(\frac{n'\pi}{L_y}y\right) dy \\ &= \begin{cases} -i \frac{2nn'}{n^2 - n'^2} [1 - (-1)^{n+n'}], & n \neq n' \\ 0, & n = n' \end{cases} \end{aligned} \quad (21)$$

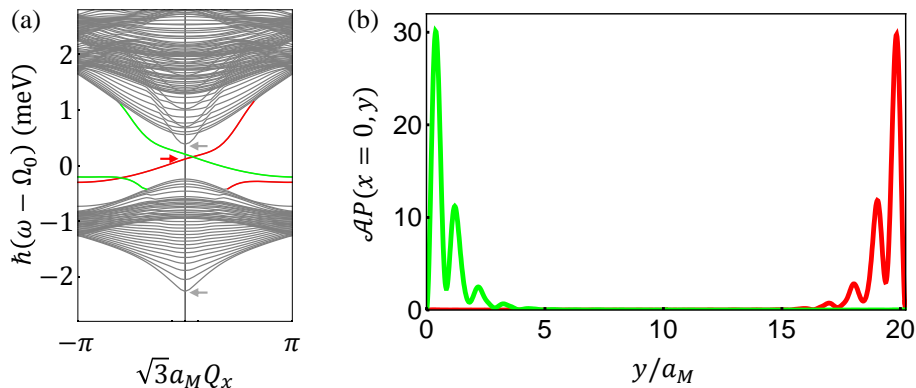


FIG. 7. (color online). (a) Same figure as Fig. 3(b) in the main text. The stripe width L_y is $20.22a_M$ and the vector \mathbf{l} is taken to be $(0,0.1)a_M$. (b) Green (red) curve presents the spatial distribution of the $Q_x = 0$ states on the green (red) line in (a).

$$F(z) = \frac{1}{L_y} \int_0^{L_y} \exp(i \frac{z\pi}{L_y} y) dy \quad (22)$$

$$= \begin{cases} i \frac{1-(-1)^z}{z\pi}, & z \neq 0 \\ 1, & z = 0 \end{cases}.$$

The energy spectrum for the stripe geometry is obtained by diagonalizing the Hamiltonian matrix with a proper truncation in parameters Q_x and n . Because of the moiré potential, Q_x reduced to the 1D Brillouin zone $(-\frac{\pi}{\sqrt{3}a_M}, \frac{\pi}{\sqrt{3}a_M})$ is a good quantum number. We define the spatial distribution of exciton state as:

$$P(\mathbf{r}) = |\psi_{K_+}(\mathbf{r})|^2 + |\psi_{K_-}(\mathbf{r})|^2, \quad (23)$$

where $(\psi_{K_+}(\mathbf{r}), \psi_{K_-}(\mathbf{r}))$ represents valley spinor wave function of exciton.

Fig. 7(a) reproduces Fig. 3(b) in the main text. The red and blue curves highlight in-gap states, which are localized on opposite edges as demonstrated in Fig. 7(b). The localization length of edge states is governed by a_M , which is much bigger than the lattice constant. The real edge on atomic length scale can be complicated. However, it should play a minor role on the exciton edge states because of different length scales.

OPTICAL RESPONSE OF EDGE STATES

Light-matter coupling is theoretically described by:

$$\delta H = - \int d\mathbf{r} \mathbf{A} \cdot \mathbf{j}(\mathbf{r}), \quad (24)$$

where \mathbf{j} is the current operator of matter, and \mathbf{A} is the vector potential of light. We assume that light propagates perpendicular to the 2D system under study. Therefore, \mathbf{A} is in the 2D plane, and is independent of the 2D position \mathbf{r} .

Using the Kubo formula, we can express the spatially resolved optical conductivity as follows:

$$\sigma_{ab}(\omega, \mathbf{r}) = \frac{i}{\omega} \sum_{\chi} \frac{\langle G | j_a(\mathbf{r}) | \chi \rangle \langle \chi | \int d\mathbf{r}' j_b(\mathbf{r}') | G \rangle}{\hbar(\omega - \omega_{\chi}) + i\eta}, \quad (25)$$

where $|G\rangle$ and $|\chi\rangle$ respectively represent ground state and excited states. Equation (25) describes the optical response at position \mathbf{r} to a spatially *uniform* electromagnetic field, and ω is assumed to be at positive frequency.

It is instructive to consider the scaling of $\sigma(\mathbf{r})$ as a function of the spatial extension W over which the exciton center-of-mass wave function $|\chi\rangle$ spreads. While the optical matrix element $\langle G | j_a(\mathbf{r}) | \chi \rangle$ scales as $1/\sqrt{W}$ because $|\chi\rangle$ is normalized, the spatial integration over \mathbf{r}' in (25) results in an extra factor W . Therefore, the local optical conductivity $\sigma(\mathbf{r})$ is an *intensive* quantity with respect to W . This scaling analysis suggests that edge states with a small lateral spatial extension can have a local optical response comparable in magnitude to that of the bulk state. The explicit calculation below agrees with this reasoning.

To study the optical response of a finite-width stripe, we make the following Fourier transformation:

$$\mathbf{j}(\mathbf{r}) = \frac{1}{A} \sum_{Q_x, n} \sqrt{2} \sin(\frac{n\pi}{L_y} y) e^{-iQ_x x} \mathbf{j}(Q_x, n), \quad (26)$$

where y extends from 0 to L_y , and n denotes positive integers.

We are interested in the variation of the optical response in y direction due to the edge states. Thus, the

optical conductivity is averaged over x direction,

$$\begin{aligned}
& \sigma_{ab}(\omega, y) \\
&= \frac{1}{L_x} \int dx \sigma_{ab}(\omega, \mathbf{r}) \\
&= \frac{i}{\omega \mathcal{A}} \sum_{\chi} \left\{ \left[\sum_n \sqrt{2} \sin\left(\frac{n\pi}{L_y} y\right) \langle G | j_a(Q_x = 0, n) | \chi \rangle \right] \right. \\
&\quad \times \left[\sum_{n' \in \text{odd}} \frac{2\sqrt{2}}{n'\pi} \langle \chi | j_b(Q'_x = 0, n') | G \rangle \right] \\
&\quad \times \left. \frac{1}{\hbar(\omega - \omega_{\chi}) + i\eta} \right\}. \tag{27}
\end{aligned}$$

$|\chi\rangle$ can be expressed in terms of the basis states in Eq. (18):

$$|\chi\rangle = \sum_{Q_x, n, \alpha} \chi_{Q_x, n, \alpha} |Q_x, n, \alpha\rangle, \tag{28}$$

where $\chi_{Q_x, n, \alpha}$ represents the eigen vectors of the Hamiltonian in Eq. (19).

To proceed, we make the following approximation:

$$\begin{aligned}
& \langle Q_x, n, \alpha | \mathbf{j}(Q_x, n) | G \rangle \\
& \approx \langle Q_x = 0, n = 1, \alpha | \mathbf{j}(Q_x = 0, n = 1) | G \rangle, \tag{29}
\end{aligned}$$

which is a small-momentum expansion of the optical matrix element to zeroth order.

Finally, we obtain the expression that is suitable for numerical calculation:

$$\begin{aligned}
\sigma_{xx}(\omega, y) &\approx \frac{\text{Re}\sigma_{xx}^{(0)}(\Omega_0)}{2} \sum_{\chi} \left\{ \left[\sum_{n, \alpha} \sqrt{2} \sin\left(\frac{n\pi}{L_y} y\right) \chi_{0, n, \alpha} \right] \right. \\
&\quad \times \left. \left[\sum_{n' \in \text{odd}, \alpha'} \frac{2\sqrt{2}}{n'\pi} \chi_{0, n', \alpha'}^* \right] \frac{i\eta}{\hbar(\omega - \omega_{\chi}) + i\eta} \right\}, \tag{30}
\end{aligned}$$

where $\text{Re}\sigma_{xx}^{(0)}(\Omega_0)$ is the A exciton optical conductivity peak in the bulk and in the absence of Zeeman field.

For bulk states, we assume that their optical response is spatially uniform. Because of the Zeeman field, the A exciton peak splits into two peaks around Ω_0 . The optical conductivity from bulk states is illustrated in Fig. 4(a) of the main text. The broadening factor η is chosen to be 1meV.

The optical response due to edge states is calculated using Eq. (30). The overall optical conductivity including contribution from both bulk and edge states is shown in Fig. 4(b) of the main text. The edge states have a strong optical response near the edge. Based on numerical results, we find that the *maximum* local optical conductivity due to one edge state is about $0.19\text{Re}\sigma_{xx}^{(0)}(\Omega_0)$, which is comparable in magnitude to that of the bulk optical response. Note that we have used a broadening factor η (1meV) that exceeds the bulk exciton band gap (see Fig. 7(a)). Nevertheless, the enhancement of the optical response near the edge is clearly visible.

Exciton states have a finite lifetime due to exciton-light coupling, which leads to intrinsic energy broadening. In our study, this intrinsic broadening is phenomenologically captured by the parameter η .